

# Transition characteristics and electron kinetics in microhollow cathode discharges

Cite as: J. Appl. Phys. **129**, 023302 (2021); <https://doi.org/10.1063/5.0033282>

Submitted: 14 October 2020 . Accepted: 18 December 2020 . Published Online: 08 January 2021

 Yangyang Fu,  Bocong Zheng,  Peng Zhang,  Qi Hua Fan, and  John P. Verboncoeur



View Online



Export Citation



CrossMark



## Your Qubits. Measured.

Meet the next generation of quantum analyzers

- Readout for up to 64 qubits
- Operation at up to 8.5 GHz, mixer-calibration-free
- Signal optimization with minimal latency

Find out more



# Transition characteristics and electron kinetics in microhollow cathode discharges

Cite as: J. Appl. Phys. 129, 023302 (2021); doi: 10.1063/5.0033282

Submitted: 14 October 2020 · Accepted: 18 December 2020 ·

Published Online: 8 January 2021



Yangyang Fu,<sup>1,2,a)</sup> Bocong Zheng,<sup>3,a)</sup> Peng Zhang,<sup>2</sup> Qi Hua Fan,<sup>2,3,4</sup> and John P. Verboncoeur<sup>1,2</sup>

## AFFILIATIONS

<sup>1</sup>Department of Computational Mathematics, Science and Engineering, Michigan State University, East Lansing, Michigan 48824, USA

<sup>2</sup>Department of Electrical and Computer Engineering, Michigan State University, East Lansing, Michigan 48824, USA

<sup>3</sup>Fraunhofer Center for Coatings and Diamond Technologies, Michigan State University, East Lansing, Michigan 48824, USA

<sup>4</sup>Department of Chemical Engineering and Material Science, Michigan State University, East Lansing, Michigan 48824, USA

**Note:** This paper is part of the Special Topic on Fundamentals and Applications of Atmospheric Pressure Plasmas.

**a) Authors to whom correspondence should be addressed:** fuyangya@msu.edu and bzheng@fraunhofer.org

## ABSTRACT

We demonstrate the transition characteristics and electron kinetics of microdischarges in a microgap with a cathode having microstructures using two-dimensional particle-in-cell/Monte Carlo collision (2d3v) simulations. It is found that the microdischarge is inside the hollow cavity at lower pressures, forming microhollow cathode discharges (MHCDs), while the dominant discharge moves outside the cavity at higher pressures, locating above the cathode rectangular protrusion tip. The spatial distributions of the microdischarge parameters (e.g., electric potential and electron density) are presented by capturing the transition characteristics. The electron kinetics of the microdischarges are examined based on the moment analysis of the electron Boltzmann equation. The collisional and non-collisional components of the electron power absorption are decomposed, which were seldomly investigated for microdischarges previously. The results provide fundamental insights into MHCD formation with a structured electrode at varying pressure conditions, which could be beneficial for the design and fabrication of microplasma devices in practical applications.

Published under license by AIP Publishing. <https://doi.org/10.1063/5.0033282>

## I. INTRODUCTION

Microdischarges have received growing attention during the past few decades due to their widespread applications, such as light sources, lasers, spectroscopy, surface processing, and biomedicine.<sup>1–5</sup> Microplasma sources have been developed by using surface dielectric barrier discharges,<sup>6,7</sup> microplasma jets,<sup>8–10</sup> atmospheric pressure glow discharges,<sup>11,12</sup> microhollow cathode discharges (MHCDs),<sup>13–16</sup> and so on.<sup>17–23</sup> Among the developed microdischarge devices, MHCDs have the advantages of higher concentrations of electrons and ions, lower breakdown and operating voltages, and high electro-optical conversion efficiencies compared with traditional normal glow discharges.<sup>24–26</sup> At present, precise diagnostics of MHCDs are still challenging due to the largely reduced dimension. Traditional direct measurements, such as the probe methods, can hardly be utilized, and non-invasive techniques, such as the optical spectrum,

mostly provide only spatially averaged information. While experiments provide the essential macroscopic characteristics, numerical simulations are used to reveal more fundamental microscopic mechanisms of the hollow cathode discharges.<sup>27–32</sup>

The discharges with a hollow cathode are not necessarily localized inside the hollow cathode, which depends on, but is not limited to, the electrical parameters (e.g., external circuit), gas pressure, and hollow cathode geometrical sizes.<sup>33–36</sup> Therefore, one can expect transition processes (which could be abrupt) in MHCDs when the parameters are changed continuously.<sup>37,38</sup> Stark and Schoenbach investigated different modes in hollow cathode discharges by measuring the voltage–current characteristics and light emissions.<sup>39</sup> Based on a fluid model and by tuning the discharge current, Boeuf *et al.* investigated the transition from a xenon glow discharge localized inside the hollow cathode to a glow discharge spreading along the outer cathode surface in a microhollow cathode

discharge.<sup>40</sup> By using particle-in-cell/Monte Carlo collision (PIC/MCC) simulations, Kim *et al.* found that the electron energy probability function (EPPF) evolves from the Druyvesteyn type in the early stages of the discharge into a two (or three) temperature distribution when the steady state is reached.<sup>41</sup> Although the discharge characteristics in MHCDs have been extensively studied, understanding the fundamental mechanisms is still far from complete. Particularly for practical applications, MHCD behaviors could be largely modulated by the varying discharge conditions, which requires further investigations.

In this work, by using the two-dimensional PIC/MCC (2d3v) simulations, we demonstrate the transition characteristics and the corresponding electron kinetics in an argon MHCD when the pressure changes. The gas pressure is tuned from 20 Torr to 150 Torr (1 Torr = 133.33 Pa) for a given two-dimensional Cartesian discharge geometry. We consider the MHCD array designed with multiple cathode rectangular surface protrusions and simulate the discharge by selecting one of the periodic domains ( $150 \times 200 \mu\text{m}^2$ ), which incorporates the rectangular protrusion ( $50 \times 150 \mu\text{m}^2$ ). We observed that the microdischarges are inside the hollow cavity at lower pressures, while they mostly transit to the region between the cathode protrusion tip and the anode as pressure increases. We present the spatial distributions of the fundamental microdischarge parameters, including the plasma density, electric field, electron power absorption, and EPPF. In this work, we also provide a comprehensive kinetic analysis of the MHCD during the transition at different pressures, which could be beneficial for designing microdischarge array devices for practical applications. We organize the rest of the paper as follows. In Sec. II, we describe the microdischarge model, including the microgap geometry and discharge condition; we also provide the computational method and simulation details. In Sec. III, we first demonstrate the transition characteristics of the MHCD by showing the spatial distributions of the electron density at different pressures. Next, we briefly introduce theoretical background of the moment analysis of the electron Boltzmann equation. Then, by choosing two typical cases at 30 Torr and 150 Torr, we analyze the electron kinetic behaviors with the spatial distributions of the diagnosed fundamental parameters. In Sec. IV, we give the concluding remarks.

## II. MODEL DESCRIPTION

### A. Discharge model

The schematic of the microgap in Cartesian geometry ( $xy$ ) is shown in Fig. 1. The microgap consists of the planar anode and the cathode designed with multiple rectangular surface metal protrusions. A direct-current voltage  $V_{dc}$  is applied to the anode through a ballast resistor  $R_b$  and the cathode is grounded.  $d_1$  and  $d_2$  are the longest and the shortest gap distances, respectively;  $w_1$  and  $w_2$  are the cavity and protrusion widths, respectively. In this work,  $V_{dc} = 500$  V,  $R_b = 100$  k $\Omega$ ,  $d_1 = 200 \mu\text{m}$ ,  $d_2 = 50 \mu\text{m}$ ,  $w_1 = 100 \mu\text{m}$ , and  $w_2 = 50 \mu\text{m}$ . The ion-impact secondary electron emission from the cathode is considered and the emission coefficient is 0.1 for argon ions. The cathode microstructure is periodically arrayed in the  $x$  direction. To distinguish the different discharge regions, we

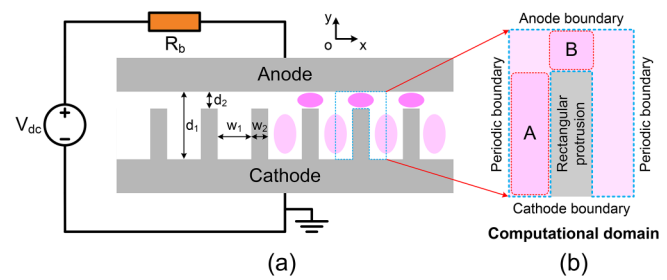


**FIG. 1.** (a) Schematic of the microgap with the structured cathode in Cartesian geometry ( $xy$ );  $V_{dc}$  is the applied voltage and  $R_b$  is the ballast resistor;  $d_1$  and  $d_2$  are the longest and the shortest gap distances, respectively;  $w_1$  and  $w_2$  are the cavity and protrusion widths, respectively. (b) The computational domain incorporates the rectangular protrusion and has two periodic boundaries on the left and right sides, respectively; A and B denote the cavity and volume discharge regions. In the simulation,  $V_{dc} = 500$  V,  $R_b = 100$  k $\Omega$ ,  $d_1 = 200 \mu\text{m}$ ,  $d_2 = 50 \mu\text{m}$ ,  $w_1 = 100 \mu\text{m}$ , and  $w_2 = 50 \mu\text{m}$ .

label A and B to denote the cavity and volume discharge regions, respectively. Here, considering there are many arrays inside the gap, we simulated only one of the periodic regions, and the outside edge effect on the discharge is not studied since the periodic boundary condition is used. The computational domain incorporates the rectangular protrusion and has two periodic boundaries on the left and right sides, respectively.

### B. PIC/MCC simulation

The two-dimensional PIC/MCC simulations are based on our ASTRA code<sup>42–44</sup> (see supplementary materials in Ref. 42 for the code description and the code benchmark with Turner *et al.*<sup>45</sup>). The simulations are performed with argon at 300 K, accounting for three electron-neutral collisions (elastic, excitation, and ionization scattering) and two ion-neutral collisions (isotropic and backward scattering) with the same cross-section data used in Ref. 44. Note that the reaction set is fixed for all cases, and, thus, even at high pressure, the stepwise ionization and three-body collisions are not considered, which may convert the dominant ion species from atomic to molecular above several tens of Torr.<sup>46</sup> The impact of the reaction kinetics could be inferred from the fluid and global model simulations;<sup>47,48</sup> here, we mainly focus on the fundamental electron kinetics during the discharge transitions.

In the simulations, the time step is  $\Delta t = 0.2$  ps; the mesh grid is uniform, and the grid size is  $\Delta d = \Delta x = \Delta y = 2 \mu\text{m}$ . Since we adopted an implicit algorithm and an energy conservation scheme for all the simulations, the major constraints on resolving the Debye length and the electron plasma period are eliminated.<sup>49,50</sup> To fulfill the particle Courant criterion, if the electron travel distance  $\Delta s$  during  $\Delta t$  is greater than  $\Delta d$ , the time step for this electron is split and the electron is advanced twice with  $0.5\Delta t$ . This procedure iteratively repeats until  $\Delta s < \Delta d$ , which is essential for the very high-energy electrons. The typical convergence time is about hundreds of nanoseconds for the lowest pressure used here, which is also generally smaller as the pressure increases in the studied cases.

### III. RESULTS AND DISCUSSION

#### A. Transition characteristics at different pressures

We performed the PIC/MCC simulations for the microgap geometry as the gas pressure  $p$  increases from 20 to 150 Torr and observed the transition characteristics of the microdischarge. Figure 2 shows the spatial distributions of the electron density at steady state. The maximum densities are  $3.2 \times 10^{20}$ ,  $4.7 \times 10^{20}$ ,  $5.8 \times 10^{20}$ , and  $3.1 \times 10^{20} \text{ m}^{-3}$  for 20, 30, 50, and 150 Torr, respectively. At lower pressures ( $p = 20 \sim 50$  Torr), the discharges are all inside the cavity. As the pressure increases, the discharge can penetrate deeper toward the cavity bottom with increased electron densities. The maximum density is at the center of the hollow cavity ( $x = 0 \text{ }\mu\text{m}$  and  $y = 150 \text{ }\mu\text{m}$ ). At the high pressure ( $p = 150$  Torr), the discharge is mainly between the anode and the protrusion tip, having two side discharges inside the cavity. However, the discharge inside the cavity does not have the maximum density at the  $x = 0 \text{ }\mu\text{m}$  or  $x = 150 \text{ }\mu\text{m}$ , which indicates that the discharges from the neighboring protrusion sidewall are separate inside the cavity. Without the overlapping of the negative glow region in the  $x$  direction, the hollow cathode discharge mode cannot occur, which explains the lowest electron density at the highest pressure among the studied cases.

The transition characteristics are consistent with the previous experimental trends that the microhollow cathode discharge forms when the product of gas pressure and hollow width  $pw_1$  is within a

limited range, i.e.,  $pw_1 = 0.026 \sim 10$  Torr cm for argon.<sup>51</sup> Note that the lowest value was just a theoretical value based on the assumption that the mean free path for ionization is not larger than the hollow cathode diameter; from the experimental data by Schoenbach *et al.*,<sup>52</sup> the lowest value is about 0.53 Torr cm ( $p = 7.5$  Torr), which is 20 times the theoretical value. As for the upper limit, Schoenbach's experimental studies suggest approximately  $pw_1 = 5$  Torr cm for an argon MHCD.<sup>24</sup> Note that the  $pw_1$  range from one experimental setup may not be universal and could be affected by other geometry parameters, such as  $d_1$ ,  $d_2$ , and  $w_2$  [see Fig. 1(a)]. These parameters can also impact the discharge behaviors and could likely alter the existing range of the hollow cathode discharge mode, which has not been characterized yet. Here in our cases, the hollow cathode discharge cannot form when  $pw_1$  is higher than 1.5 Torr cm, which is within the range of the experimental results. At the lowest pressure case (20 Torr), we still observe the hollow cathode discharge with  $pw_1 = 0.2$  Torr cm. Although the exact boundaries could be different, our simulations show the MHCD having  $pw_1$  at the same order of magnitude. Additionally, the simulation results confirmed that the MHCD exists when  $pw_1$  is within a certain range and varies no larger than one order of magnitude, which is consistent with the experimental results.

Note that for a given hollow cathode structure, the hollow cathode discharge cannot form if the gas pressure is too low, especially when the sheath width is larger than the cavity dimension.<sup>33</sup> For a macroscopic case, the hollow cathode effect with pendulum electrons usually occurs in certain pressure regimes, which was also experimentally confirmed.<sup>53</sup> On the other hand, if the gas pressure is too high, the conventional hollow cathode discharge cannot form since the characteristic length, such as the electron mean free path, is too small to obtain a pendulum effect. Also note that, due to geometrical difference, the microdischarge generated with coplanar circular sandwich microstructure arrays can still form inside the cavity without the pendulum effect but with a ring structure.<sup>40,54</sup> Generally, the microhollow cathode discharge with a high concentration of the electron density at the center of the microcavity can only form within a certain pressure range.

Figure 3 shows the spatial distributions of the electric potential at different pressures. The electric potential inside the hollow cavity is mostly equipotential with the anode, showing the formation of a typical virtual anode. For the lower pressure cases, the electric potential is not much distorted between the anode and the rectangular protrusion tip, and the discharges have a relatively wider cathode potential drop region, while at higher pressures, the cathode voltage drops in a narrower distance apart from the cathode surface. As the pressure increases, the gap voltage decreases, which, correspondingly, indicates that the total discharge current increases. Although the discharge current is the largest at the highest pressure, the electron density is still the lowest, since the discharge is not a typical MHCD. It is worth mentioning that the similarity of the single hollow cathode discharge in Cartesian and cylindrical geometries is confirmed by Lafleur *et al.*<sup>55</sup> For the characterization of microplasmas around an array of micro trenches in Cartesian geometry, the discharge behavior could be different from the conventional hollow cathode discharge and more complex, which can be affected by more geometrical factors (e.g., the width and spacing of the designed microstructures).

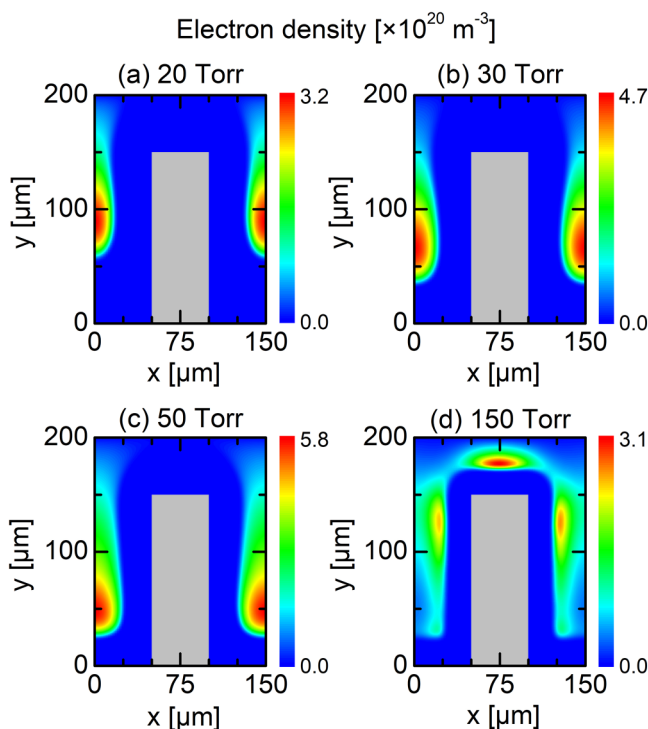


FIG. 2. Spatial distributions of the electron density at different pressures. (a) 20 Torr, (b) 30 Torr, (c) 50 Torr, and (d) 150 Torr.

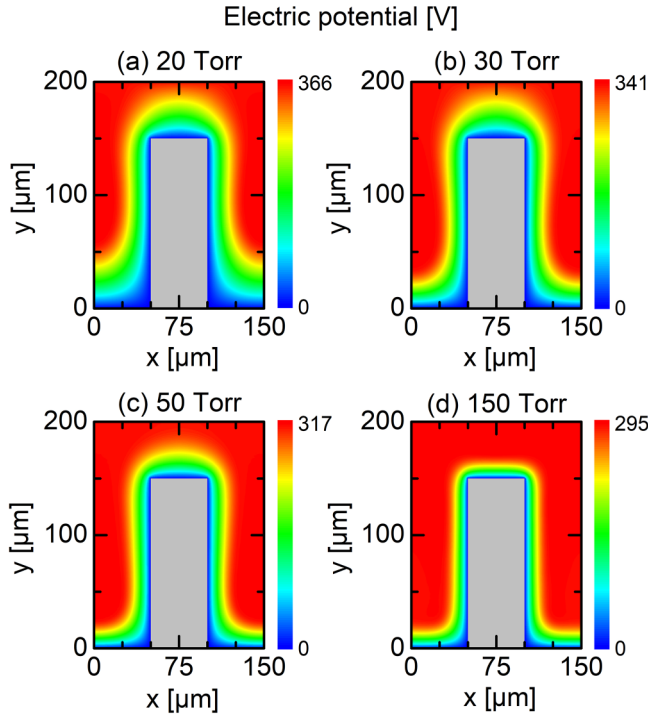


FIG. 3. Spatial distributions of the electric potential at different pressures. (a) 20 Torr, (b) 30 Torr, (c) 50 Torr, and (d) 150 Torr.

## B. Analysis on the electron kinetics

Here, we briefly introduce the theoretical background of the moment analysis of the electron Boltzmann equation, which is theoretically rigorous and has been successfully applied in previous studies.<sup>42,55–58</sup> Let us start with the electron Boltzmann equation, which is expressed as

$$\frac{\partial f_e}{\partial t} + \mathbf{v} \cdot \nabla_{\mathbf{x}} f_e - \frac{e\mathbf{E}}{m_e} \cdot \nabla_{\mathbf{v}} f_e = \left. \frac{\partial f_e}{\partial t} \right|_{coll}, \quad (1)$$

where  $f_e = f(\mathbf{x}, \mathbf{v}, t)$  is the electron spatiotemporal velocity distribution,  $\mathbf{v}$  is the velocity,  $m_e$  and  $e$  are the electron mass and charge,  $t$  is the time,  $\mathbf{E}$  is the electric field, and  $(\partial f_e / \partial t)_{coll}$  is the collisional term.<sup>42</sup> Multiplying the Boltzmann equation by  $\mathbf{v}$  and integrating all terms of Eq. (1) over the velocity space, we obtain the momentum conservation equation for electrons,

$$m_e n_e \frac{\partial \mathbf{u}_e}{\partial t} + m_e (\mathbf{\Gamma}_e \cdot \nabla) \mathbf{u}_e = -en_e \mathbf{E} - \nabla \cdot \vec{\Pi} + \left( \frac{\partial \rho_e}{\partial t} \right)_{coll}, \quad (2)$$

where  $n_e$ ,  $\mathbf{u}_e$ ,  $\mathbf{\Gamma}_e$ ,  $\vec{\Pi}$ , and  $(\partial \rho_e / \partial t)_{coll}$  are the electron density, drift velocity, drift flux, pressure tensor, and change of momentum due to collisions, respectively. Since the electric field here is on the  $xy$

plane, the electron power density can be written as

$$P_e(x, y, t) = \mathbf{J}_e \cdot \mathbf{E} = J_{ex} E_x + J_{ey} E_y, \quad (3)$$

where  $\mathbf{J}_e = -en_e \mathbf{u}_e$  is the electron current density on the  $xy$  plane. Multiplying each component of Eq. (2) in different directions with the corresponding drift velocities, we obtain the electron energy conservation equations in the  $x$  and  $y$  directions. The sum of these equations gives the total electron mechanical energy conservation equation,

$$P_e = P_{acc} + P_{in} + P_{press} + P_{coll}, \quad (4)$$

where

$$\begin{aligned} P_{acc} &= m_e n_e \sum_i u_{ei} \frac{\partial u_{ei}}{\partial t}, \\ P_{in} &= m_e \sum_i u_{ei} \left( \Gamma_{ex} \frac{\partial u_{ei}}{\partial x} + \Gamma_{ey} \frac{\partial u_{ei}}{\partial y} \right), \\ P_{press} &= \sum_i u_{ei} \left( \frac{\partial \Pi_{exi}}{\partial x} + \frac{\partial \Pi_{eyi}}{\partial y} \right), \\ P_{coll} &= - \sum_i u_{ei} \left( \frac{\partial \rho_{ei}}{\partial t} \right)_{coll} \end{aligned} \quad (5)$$

are the electron power absorption components due to the acceleration term, the inertial term, the pressure-induced effect, and the collisional dynamics;  $i = x$  and  $y$  is the axis coordinate. Note that the contribution of the acceleration term is zero ( $P_{acc} = 0$ ) for dc discharges at steady state.

In the following, we choose  $p = 30$  Torr and 150 Torr as typical cases and compared the fundamental electron kinetics. We first show in Fig. 4 the spatial distributions of the electric field in the  $x$  and  $y$  directions when the discharges are at steady state. The electric field components are on the order of  $10^7$  V m<sup>-1</sup> and the field magnitudes at 30 Torr are generally less than that at 150 Torr. The electric field is determined by the electrostatic and space charge fields, which may behave differently in space and strength at different pressures. At higher pressures, the sheath width is reduced, and the electric potential drops within a shorter distance (see Fig. 3), which generally leads to a stronger field strength. For both cases, inside the cavity ( $50 \mu\text{m} \leq y \leq 150 \mu\text{m}$ ), the  $E_x$  component dominates in the vicinity of the protrusion sidewall and the field directions are mostly perpendicular to the protrusion surface when the  $E_y$  component is negligible. The  $E_y$  component is prominent either near the hollow cathode bottom or on the tip of the surface protrusion. Note that the electrostatic field mainly contributes to the field strength at the protrusion tip, which generally cannot penetrate deeply into the hollow cathode because of the shielding effect.<sup>34</sup> Thus, at 30 Torr, the electric field  $E_y$  inside the cavity is mainly due to the space charge effect. The relatively high electric field around the protrusion corner, where the local plasma density is also low, is due to the fringing field effect. At 150 Torr, the  $E_y$  component above the protrusion tip becomes even higher, and the strong electric field is mostly inside the sheath, which is



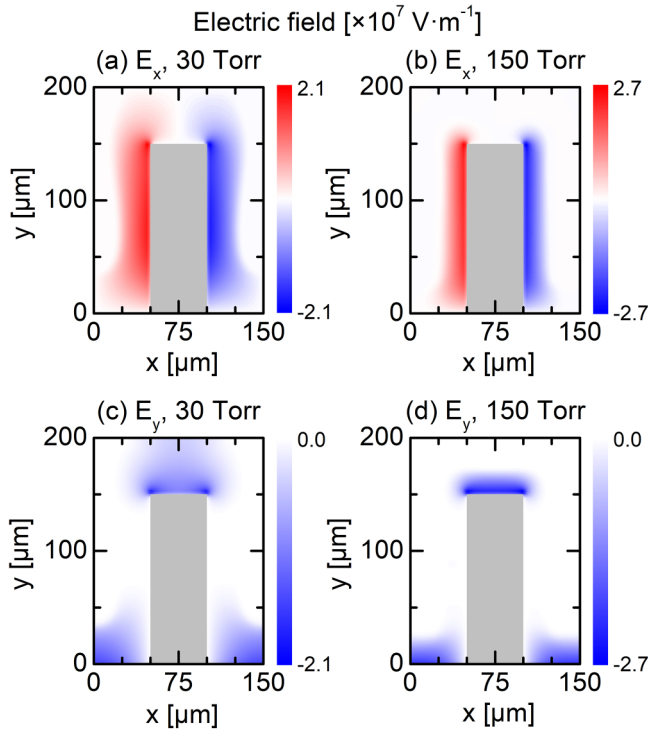


**FIG. 4.** Spatial distributions of the electric field in the  $x$  and  $y$  directions. (a)  $E_x$  at 30 Torr, (b)  $E_x$  at 150 Torr, (c)  $E_y$  at 30 Torr, and (d)  $E_y$  at 150 Torr.

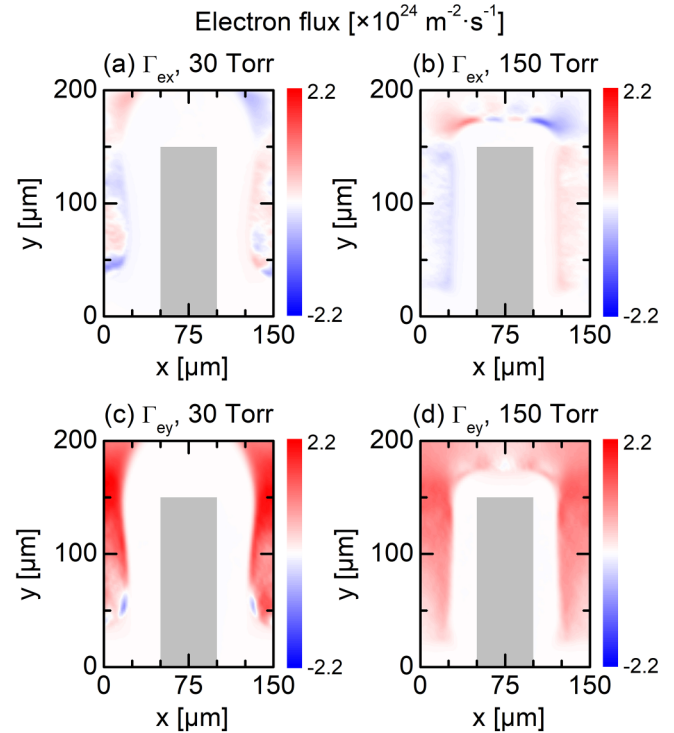


**FIG. 5.** Spatial distributions of the total electron flux in the  $x$  and  $y$  directions. (a)  $\Gamma_{ex}$  at 30 Torr, (b)  $\Gamma_{ex}$  at 150 Torr, (c)  $\Gamma_{ey}$  at 30 Torr, and (d)  $\Gamma_{ey}$  at 150 Torr.

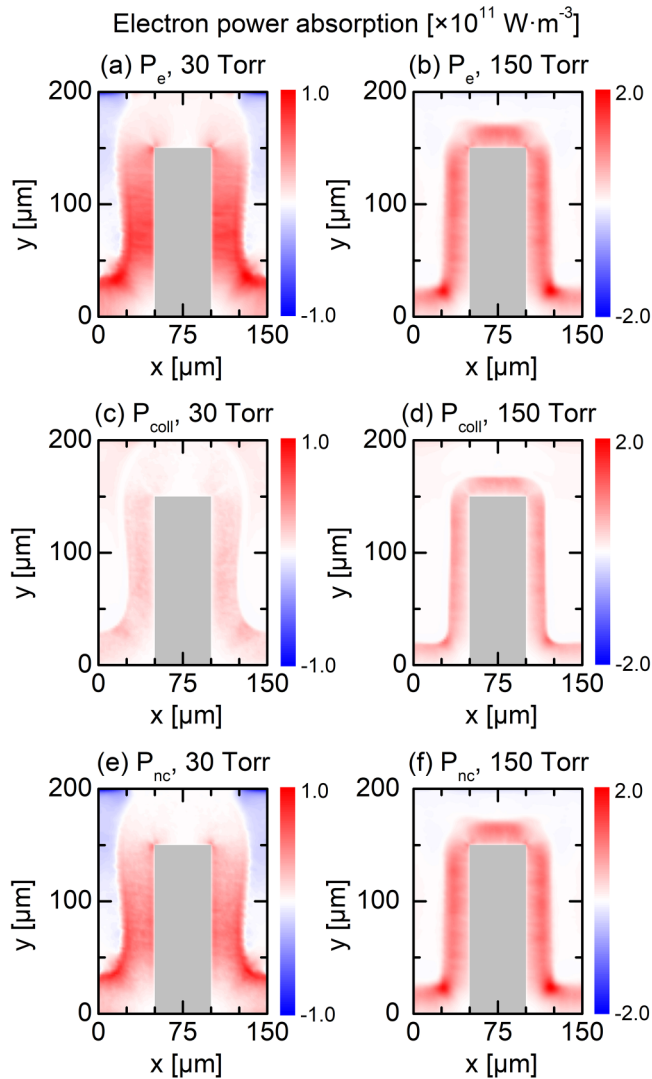
due to the space charge effect in the sheath and the quasi-neutral plasma elsewhere.

Figure 5 shows the spatial distributions of the electron flux in the  $x$  and  $y$  directions. Note that for all plots, the color bar is set to be symmetric and within the same range, referring to the maximum value in the  $y$  direction. For both cases, the electron flux is negligible inside the plasma sheath where the ion species are dominant. Since the discharge is mainly inside the cavity at 30 Torr, the electron flux is also negligible in the region between the anode and the protrusion. We can see that in Fig. 5(a) the electron flux is bidirectional inside the cavity at 30 Torr. This is due to the diffusion flux induced by the density gradient, flowing from the discharge bulk to the cathode, and the beamlike secondary electron flux, flowing from the cathode to the bulk. In Fig. 5(a), inside the cavity, the former is surrounded by the later components. In Fig. 5(b), it is outward from the protrusion surface at 150 Torr, which indicates that the secondary electron flux dominates. The generated beam electrons largely enhance the ionization process and increase the plasma density. In Figs. 5(c) and 5(d), we see that the electron flux components in the  $y$  direction are larger than that in the  $x$  direction, showing strong electron fluxes toward the anode.

We show in Fig. 6 the spatial distributions of the electron power absorption  $P_e = \mathbf{J}_e \cdot \mathbf{E}$ , which is decomposed into the collisional heating  $P_{coll}$  and the non-collisional heating component  $P_{nc}$ . Since  $P_{acc} = 0$  at a steady state in our cases, the non-collisional electron

heating component is  $P_{nc} = P_{in} + P_{press}$  [see Eq. (5)], which is due to the electron inertia and the pressure-induced heating.<sup>42,58</sup> In Figs. 6(a) and 6(b), the total electron power absorption is significant in the sheath region at both 30 Torr and 150 Torr, whereas the electron cooling components are not obviously observed. The collisional heating component is always positive and mostly inside the sheath region, as shown in Figs. 6(c) and 6(d). However, the collisional heating is generally less than the non-collisional heating component, as shown in Figs. 6(e) and 6(f). The collisional heating in the sheath mainly emanates from the collisions between the secondary electrons and neutral gas. According to Ref. 59, the electron mean free path is  $\sim 10 \mu\text{m}$  in argon at 30 Torr, indicating that the secondary electrons can experience several collisions when traveling across the sheath region. In Figs. 6(e) and 6(f), the non-collisional heating is also the strongest inside the sheath, which is mostly from the secondary electron heating. The secondary electrons can also directly gain energy from the sheath field, and this process does not necessarily require collisions, which is attributed to the non-collisional heating component.

Since the electron density  $n_e$  and the electron flux  $\Gamma_e$  are already shown in Figs. 3 and 5, respectively, we further calculate the electron velocity components through  $u_{ei} = \Gamma_{ei}/n_e$  ( $i = x$  and  $y$ ). Figure 7 shows the electron mean velocity in the  $x$  and  $y$  directions at 30 Torr and 150 Torr. Note that here the electron velocity  $u_e$  is the mean velocity at the corresponding space point, which is a



**FIG. 6.** Spatial distributions of the total electron power absorption  $P_e$ , collisional electron heating component  $P_{coll}$ , and non-collisional heating component  $P_{nc}$ . (a)  $P_e$  at 30 Torr, (b)  $P_e$  at 150 Torr, (c)  $P_{coll}$  at 30 Torr, (d)  $P_{coll}$  at 150 Torr, (e)  $P_{nc}$  at 30 Torr, and (f)  $P_{nc}$  at 150 Torr.

fluidic parameter. It is observed that the spatial distributions of the electron mean velocity are similar to the electric field profiles for both the  $x$  and  $y$  components (see Figs. 4 and 7); note that the electron velocity and the electric field generally have opposite directions. According to Ref. 59, assuming the electron energy gain from the electric field balanced with the collisional loss at a steady state, we have the mean electron energy  $\bar{\epsilon}$  proportional to the electric field, i.e.,  $\bar{\epsilon} \propto eE\lambda/\sqrt{\delta}$ , where  $\lambda$  is the electron free path and assumed to be energy-independent and  $\delta$  is the mean fraction of the electron energy loss during the collision (the coefficient  $\delta$  is small, e.g.,  $\delta = 10^{-3} \sim 10^{-2}$  for inelastic collisions and

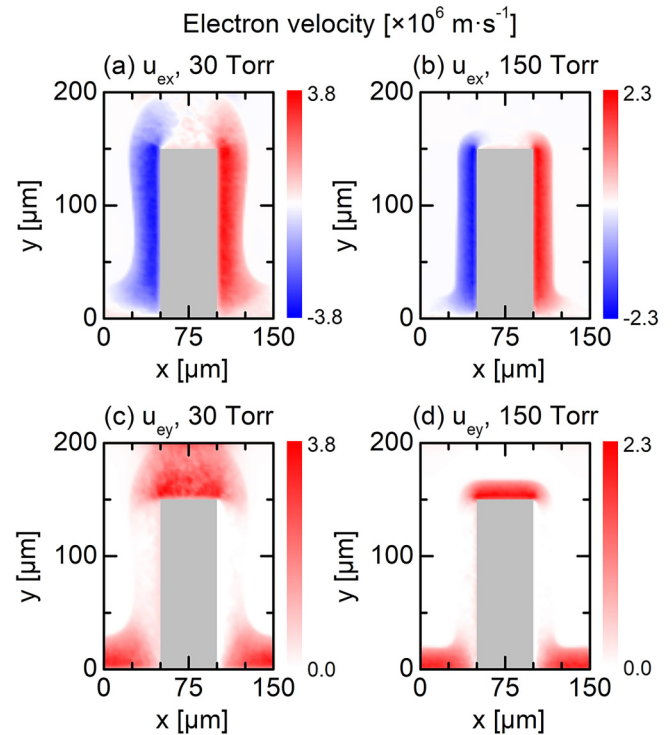


**FIG. 7.** Spatial distributions of the total electron velocity in the  $x$  and  $y$  directions. (a)  $u_{ex}$  at 30 Torr, (b)  $u_{ex}$  at 150 Torr, (c)  $u_{ey}$  at 30 Torr, and (d)  $u_{ey}$  at 150 Torr.

$\delta = 10^{-4} \sim 10^{-5}$  for elastic collisions). This relation explains why the electron mean velocity shows a similar spatial distribution to the electric field, and due to the existence of the coefficient  $\delta$ , the mean velocity is generally higher than the drift velocity. The fluid evaluation indeed reflects the value of the local approximations (e.g., local field and local energy approximations) when the microscopic kinetic information is ignored.

In Fig. 8, we present the electron impact ionization rate, which is directly calculated from the PIC/MCC simulations. The maximum ionization rates are  $1.6 \times 10^{28} \text{ m}^{-3} \text{ s}^{-1}$  and  $3.2 \times 10^{28} \text{ m}^{-3} \text{ s}^{-1}$  at 30 Torr and 150 Torr, respectively. At 30 Torr, the highest ionization rate is in the plasma bulk, whereas at 150 Torr, the strongest ionization is inside the sheath region, which is the main difference between the compared microdischarges with different collisionalities. At lower pressures (e.g., 30 Torr), the electrons gain energy mostly inside the sheath but experience energy loss ionizations elsewhere, showing the typical nonlocal electron kinetic feature. At higher pressures (e.g., 150 Torr), the sheath becomes more collisional and most of the ionization occurs inside the sheath, indicating that the electron kinetics become more local. However, the spatial discrepancy between the ionization rate and the strongest electric field near the cathode surface can still be observed, which means that the nonlocal kinetic behaviors are not eliminated even in the high-pressure discharges.

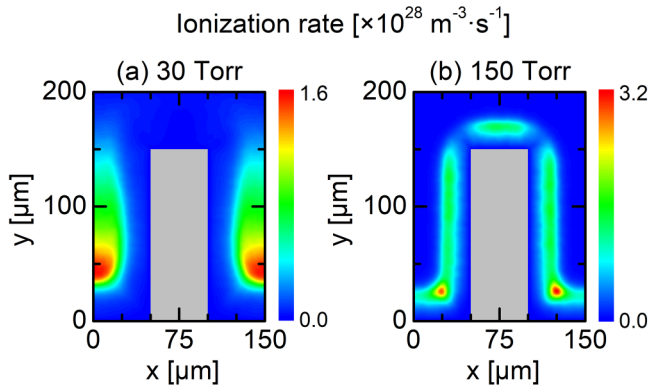


FIG. 8. Spatial distributions of the electron impact ionization rate at (a) 30 Torr and (b) 150 Torr, respectively.

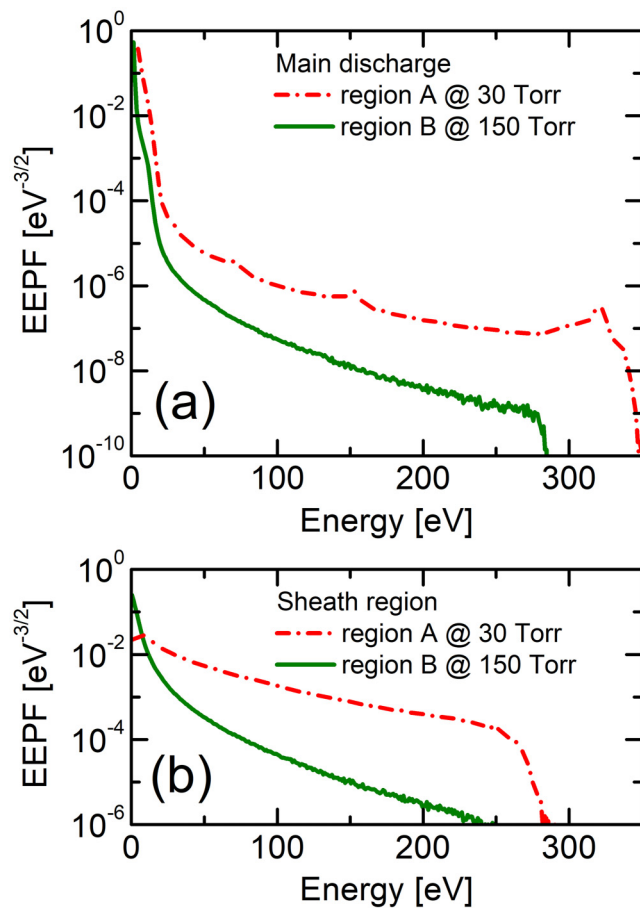


FIG. 9. Comparison of the EPPFs for discharges at 30 Torr and 150 Torr in (a) the main discharge region and (b) the corresponding sheath region, respectively.

The EPPFs are also compared in different regions of the discharges in Fig. 1(b). Figure 9(a) shows the EPPF in the main discharge region, i.e., region A at 30 Torr and region B at 150 Torr. For both cases, we observe high-energy tails, which are due to the secondary electrons traveling from the sheath to the plasma bulk. The largest electron energy can reach as high as 350 eV and 282 eV at 30 Torr and 150 Torr, respectively, very close to the maximum electric potential 351 V at 30 Torr and 291 V at 150 Torr (see Fig. 3), which are relevant to the maximum sheath voltage drop (the gap voltage plus the plasma potential). The corresponding gap voltage is 334 V and 292 V at 30 Torr and 150 Torr, respectively. At 30 Torr, the maximum electron energy is slightly higher than the gap voltage, which is due to the existing plasma potential. As shown in our previous work,<sup>43</sup> secondary electrons can gain the full potential energy and convert it to the kinetic energy while reaching the plasma bulk. This process is generally true as long as some of the electrons can travel across the sheath ballistically. At 150 Torr, the maximum electron energy is slightly smaller than the gap voltage since the electrons are more collisional. In Fig. 9(a), the high-energy tail in the EPPF at 30 Torr is more pronounced than that at 150 Torr, which is due to the larger mean free path of the secondary electrons and the population of the high-energy ballistic electrons.

Figure 9(b) shows the EPPFs in the corresponding sheath region at 30 Torr and 150 Torr. At the same level of the coordinates, the EPPFs have more pronounced boosted high-energy tails, which extend to larger than 200 eV at the level of  $10^{-6} \text{ eV}^{-3/2}$  in the coordinate. Note that here we measure only the electron energy apart from the electrode within  $20 \mu\text{m}$ , not the whole sheath with an exact boundary. The maximum counted electron energy is slightly reduced (about 10% ~ 20% less), which is because the measured secondary electrons have not gained the full potential energy. Similarly, the EPPF shows a more pronounced high-energy tail in the MHCD at 30 Torr than that in the microdischarge above the protrusion tip at 150 Torr. Particularly at 30 Torr, the number ratio between the fast electrons and slow electrons is much higher when only the sheath electrons are counted. The highly non-Maxwellian EPPFs and the presence of the beam electrons demonstrate the nonlocal electron kinetic nature in the MHCD.

#### IV. CONCLUDING REMARKS

We have demonstrated the discharge transition and the electron kinetic characteristics in an argon MHCD at different pressures by using two-dimensional PIC/MCC (2d3v) simulations. It is found that the main discharge region is inside the hollow cavity at lower pressures, while it locates at the rectangular protrusion tip at higher pressures. The electron kinetic characteristics for two typical cases are examined based on the moment analysis of the electron Boltzmann equation. The fundamental parameters, such as the electron density, electric field, and electron flux, are presented when the discharges reach the steady state. Other physical parameters, such as the electron power absorption and the electron velocity, are also analyzed. The electron power absorption is the strongest inside the sheath, which is contributed by the secondary electrons. The defined collisional heating is more obvious inside the sheath; it is always positive but generally has a smaller



magnitude compared with its non-collisional component. The dominant ionization rate at lower pressures is in the plasma bulk region, while at higher pressures, it is mostly inside the sheath region. As the pressure increases, the nonlocal electron kinetics is suppressed but not eliminated in the high-pressure discharges. The EEPF is highly non-Maxwellian and has boosted high-energy tails due to secondary electrons; the highest energy corresponds to the maximum sheath potential drop, which is determined by the gap voltage and the plasma potential. In the studied cases, the high-energy tail of the EEPF in the sheath region is more pronounced than that in the main discharge region. This work provides a microscopic analysis of the electron kinetics in the MHCD during the transition at different pressures, which is essential for understanding the discharge with irregular electrodes and designing arrayed microdischarge devices in practical applications. In this work, we consider only the ion-induced secondary electron emission from the cathode surface. However, at smaller dimensions, or if the surface roughness on the protrusion structures is additionally considered, the electric field could be largely enhanced (e.g., order of  $10^9$  V/m, entering into the field emission regime<sup>60–62</sup>), and one may expect strong field emission from the metal surface, which will be studied in our future work.

## ACKNOWLEDGMENTS

The authors are grateful to Professor Hae June Lee (Pusan National University) for his helpful comments and fruitful discussions. This work was supported by the Air Force Office of Scientific Research (Grant No. FA9550-18-1-0062), the Air Force Office of Scientific Research (Grant No. FA9550-18-1-0061), the U.S. Department of Energy Office of Fusion Energy Science (Grant No. DE-SC0001939), and the National Science Foundation (Award Nos. 1917577 and 1724941).

## DATA AVAILABILITY

The data that support the findings of this study are available from the corresponding authors upon reasonable request.

## REFERENCES

- <sup>1</sup>K. H. Schoenbach and K. Becker, *Eur. Phys. J. D* **70**, 29 (2016).
- <sup>2</sup>J. Hopwood, A. R. Hoskinson, and J. Gregorio, *Plasma Sources Sci. Technol.* **23**, 064002 (2014).
- <sup>3</sup>D. Levko and L. L. Raja, *J. Appl. Phys.* **119**, 163303 (2016).
- <sup>4</sup>A. M. Loveless and A. L. Garner, *IEEE Trans. Plasma Sci.* **45**, 574 (2017).
- <sup>5</sup>J. G. Eden, S. J. Park, J. H. Cho, M. H. Kim, T. J. Houlihan, B. Li, E. S. Kim, T. L. Kim, S. K. Lee, K. S. Kim, J. K. Yoon, S. H. Sung, P. Sun, C. M. Herring, and C. J. Wagner, *IEEE Trans. Plasma Sci.* **41**, 661 (2013).
- <sup>6</sup>A. R. Hoskinson, L. Oksuz, and N. Hershkowitz, *Appl. Phys. Lett.* **93**, 221501 (2008).
- <sup>7</sup>I. Biganzoli, R. Barni, and C. Riccardi, *J. Phys. D Appl. Phys.* **46**, 025201 (2012).
- <sup>8</sup>Y. C. Hong and H. S. Uhm, *Appl. Phys. Lett.* **89**, 221504 (2006).
- <sup>9</sup>T. Kikuchi, Y. Hasegawa, and H. Shirai, *J. Phys. D Appl. Phys.* **37**, 1537 (2004).
- <sup>10</sup>J. Benedikt, K. Focke, A. Yanguas-Gil, and A. Von Keudell, *Appl. Phys. Lett.* **89**, 251504 (2006).
- <sup>11</sup>S. I. Eliseev, A. A. Kudryavtsev, H. Liu, Z. Ning, D. Yu, and A. S. Chirtsov, *IEEE Trans. Plasma Sci.* **44**, 2536 (2016).
- <sup>12</sup>J. Shi and M. G. Kong, *Phys. Rev. Lett.* **96**, 105009 (2006).
- <sup>13</sup>K. H. Schoenbach, M. I. Moselhy, W. Shi, and R. Bentley, *J. Vac. Sci. Technol. A* **21**, 1260 (2003).
- <sup>14</sup>T. Deconinck and L. L. Raja, *Plasma Process. Polym.* **6**, 335 (2009).
- <sup>15</sup>D. D. Hsu and D. B. Graves, *J. Phys. D Appl. Phys.* **36**, 2898 (2003).
- <sup>16</sup>S. Kasri, L. William, X. Aubert, G. Lombardi, A. Tallaire, J. Achard, C. Lazzaroni, G. Bauville, M. Fleury, K. Gazeli, S. Pasquiers, and J. Santos Sousa, *Plasma Sources Sci. Technol.* **28**, 035003 (2019).
- <sup>17</sup>T. Homola, R. Krumpolec, M. Zemánek, J. Kelar, P. Synek, T. Hoder, and M. Černák, *Plasma Chem. Plasma Phys.* **37**, 1149 (2017).
- <sup>18</sup>Y. D. Korolev and N. N. Koval, *J. Phys. D Appl. Phys.* **51**, 323001 (2018).
- <sup>19</sup>O. Sakai, Y. Kishimoto, and K. Tachibana, *J. Phys. D Appl. Phys.* **38**, 431 (2005).
- <sup>20</sup>G. Nayak, Y. Du, R. Brandenburg, and P. J. Bruggeman, *Plasma Sources Sci. Technol.* **26**, 035001 (2017).
- <sup>21</sup>F. Iza, J. K. Lee, and M. G. Kong, *Phys. Rev. Lett.* **99**, 075004 (2007).
- <sup>22</sup>J. Benedikt, D. Schröder, S. Schneider, G. Willems, A. Pajdarová, J. Vlček, and V. Schulz-von der Gathen, *Plasma Source Sci. Technol.* **25**, 045013 (2016).
- <sup>23</sup>D. B. Go and A. Venkattraman, *J. Phys. D Appl. Phys.* **47**, 503001 (2014).
- <sup>24</sup>K. H. Schoenbach, R. Verhappen, T. Tesson, F. E. Peterkin, and W. W. Byszewski, *Appl. Phys. Lett.* **68**, 13 (1996).
- <sup>25</sup>L. Shang, J. Ouyang, and H. Feng, *Chin. Phys. Lett.* **27**, 065201 (2010).
- <sup>26</sup>Y. Fu, J. P. Verboncoeur, and A. J. Christlieb, *Phys. Plasmas* **24**, 103514 (2017).
- <sup>27</sup>J. Greenan, C. M. O. Mahony, D. Mariotti, and P. D. Maguire, *Plasma Sources Sci. Technol.* **20**, 025011 (2011).
- <sup>28</sup>T. Homola, V. Prukner, P. Hoffer, and M. Šimek, *Plasma Sources Sci. Technol.* **29**, 095014 (2020).
- <sup>29</sup>T. Kuschel, B. Niermann, I. Stefanović, M. Böke, N. Škoro, D. Marić, Z. Lj Petrović, and J. Winter, *Plasma Sources Sci. Technol.* **20**, 065001 (2011).
- <sup>30</sup>T. Lafleur and R. W. Boswell, *Phys. Plasmas* **19**, 023508 (2012).
- <sup>31</sup>S. He, H. Jing, Z. Zhang, J. Ouyang, and Q. Li, *J. Phys. D Appl. Phys.* **49**, 365201 (2016).
- <sup>32</sup>L. Zhang, G. Zhao, J. Wang, and Q. Han, *Phys. Plasmas* **23**, 023508 (2016).
- <sup>33</sup>K. H. Schoenbach, A. E. Habachi, W. Shi, and M. Ciocca, *Plasma Sources Sci. Technol.* **6**, 468 (1997).
- <sup>34</sup>Y. Fu, P. Zhang, J. Krek, and J. P. Verboncoeur, *Appl. Phys. Lett.* **114**, 014102 (2019).
- <sup>35</sup>A. D. White, *J. Appl. Phys.* **30**, 711 (1959).
- <sup>36</sup>M. J. Kushner, *J. Appl. Phys.* **95**, 846 (2004).
- <sup>37</sup>Y. Qin, K. Xie, Y. Zhang, and J. Ouyang, *Phys. Plasmas* **23**, 023501 (2016).
- <sup>38</sup>Y. Fu, J. P. Verboncoeur, A. J. Christlieb, and X. Wang, *Phys. Plasmas* **24**, 083516 (2017).
- <sup>39</sup>R. H. Stark and K. H. Schoenbach, *J. Appl. Phys.* **85**, 2075 (1999).
- <sup>40</sup>J. P. Boeuf, L. C. Pitchford, and K. H. Schoenbach, *Appl. Phys. Lett.* **86**, 071501 (2005).
- <sup>41</sup>G. J. Kim, F. Iza, and J. K. Lee, *J. Phys. D Appl. Phys.* **39**, 4386 (2006).
- <sup>42</sup>B. Zheng, K. Wang, T. Grotjohn, T. Schuelke, and Q. H. Fan, *Plasma Sources Sci. Technol.* **28**, 09LT03 (2019).
- <sup>43</sup>Y. Fu, B. Zheng, D.-Q. Wen, P. Zhang, Q. H. Fan, and J. P. Verboncoeur, *Plasma Sources Sci. Technol.* **29**, 09LT01 (2020).
- <sup>44</sup>B. Zheng, Y. Fu, D.-Q. Wen, K. Wang, T. Schuelke, and Q. H. Fan, *J. Phys. D Appl. Phys.* **53**, 435201 (2020).
- <sup>45</sup>M. M. Turner, A. Derzsi, Z. Donkó, D. Eremin, S. J. Kelly, T. Lafleur, and T. Mussenbrock, *Phys. Plasmas* **20**, 013507 (2013).
- <sup>46</sup>Y. Fu, J. Krek, G. M. Parsey, and J. P. Verboncoeur, *Phys. Plasmas* **25**, 033505 (2018).
- <sup>47</sup>Y. Fu, G. M. Parsey, J. P. Verboncoeur, and A. J. Christlieb, *Phys. Plasmas* **24**, 113518 (2017).
- <sup>48</sup>T. Farouk, B. Farouk, D. Staack, A. Gutsol, and A. Fridman, *Plasma Sources Sci. Technol.* **15**, 676 (2006).
- <sup>49</sup>B. I. Cohen, A. Langdon, D. W. Hewett, and R. J. Procassini, *J. Comput. Phys.* **81**, 151 (1989).

- <sup>50</sup>G. Fubiani, G. J. M. Hagelaar, J. P. Boeuf, and S. Kolev, *Phys. Plasmas* **19**, 043506 (2012).
- <sup>51</sup>H. Helm, *Z. Naturf. A* **27**, 1812 (1972).
- <sup>52</sup>K. H. Schoenbach, A. E. Habachi, M. M. Moselhy, W. Shi, and R. H. Stark, *Phys. Plasmas* **7**, 2186 (2000).
- <sup>53</sup>G. Stockhausen and M. Kock, *J. Phys. D Appl. Phys.* **34**, 1683 (2001).
- <sup>54</sup>W. Shi, R. H. Stark, and K. H. Schoenbach, *IEEE Trans. Plasma Sci.* **27**, 16 (1999).
- <sup>55</sup>T. Lafleur, P. Chabert, and J. P. Booth, *Plasma Sources Sci. Technol.* **23**, 035010 (2014).
- <sup>56</sup>J. Schulze, Z. Donkó, T. Lafleur, S. Wilczek, and R. P. Brinkmann, *Plasma Sources Sci. Technol.* **27**, 055010 (2018).
- <sup>57</sup>Y. Liu, J.-P. Booth, and P. Chabert, *Plasma Sources Sci. Technol.* **27**, 025006 (2018).
- <sup>58</sup>S. Wilczek, J. Schulze, R. P. Brinkmann, Z. Donkó, J. Trieschmann, and T. Mussenbrock, *J. Appl. Phys.* **127**, 181101 (2020).
- <sup>59</sup>Y. P. Raizer, *Gas Discharge Physics* (Springer, Berlin, 1991).
- <sup>60</sup>Y. Fu, J. Krek, P. Zhang, and J. P. Verboncoeur, *Plasma Sources Sci. Technol.* **27**, 095014 (2018).
- <sup>61</sup>R. Tirumala and D. B. Go, *Appl. Phys. Lett.* **97**, 151502 (2010).
- <sup>62</sup>D. B. Go and D. A. Pohlman, *J. Appl. Phys.* **107**, 103303 (2010).